FLSEVIER

Contents lists available at ScienceDirect

Materials Science and Engineering C

journal homepage: www.elsevier.com/locate/msec



Biocompatible nanocomposite scaffolds based on copolymer-grafted chitosan for bone tissue engineering with drug delivery capability



Samaneh Saber-Samandari ^{a,*}, Saeed Saber-Samandari ^{b,*}

- ^a Department of Chemistry, Eastern Mediterranean University, Gazimagusa, TRNC via Mersin 10, Turkey
- ^b New Technologies Research Center, Amirkabir University of Technology, Tehran, Iran

ARTICLE INFO

Article history:
Received 18 June 2016
Received in revised form 23 October 2016
Accepted 21 February 2017
Available online 22 February 2017

Keywords:
Bone
Co-polymer
Drug delivery
Graft polymerization
Hydroxyapatite
Tissue engineering

ABSTRACT

Significant efforts have been made to develop a suitable biocompatible scaffold for bone tissue engineering. In this work, a chitosan-graft-poly(acrylic acid-co-acrylamide)/hydroxyapatite nanocomposite scaffold was synthesized through a novel multi-step route. The prepared scaffolds were characterized for crystallinity, morphology, elemental analysis, chemical bonds, and pores size in their structure. The mechanical properties (i.e. compressive strength and elastic modulus) of the scaffolds were examined. Further, the biocompatibility of scaffolds was determined by MTT assays on HUGU cells. The result of cell culture experiments demonstrated that the prepared scaffolds have good cytocompatibility without any cytotoxicity, and with the incorporation of hydroxyapatite in their structure improves cell viability and proliferation. Finally, celecoxib as a model drug was efficiently loaded into the prepared scaffolds because of the large specific surface area. The in vitro release of the drug displayed a biphasic pattern with a low initial burst and a sustained release of up to 14 days. Furthermore, different release kinetic models were employed for the description of the release process. The results suggested that the prepared cytocompatible and non-toxic nanocomposite scaffolds might be efficient implants and drug carriers in bonetissue engineering.

© 2017 Elsevier B.V. All rights reserved.

1. Introduction

The typical goal of a bone tissue engineering approach is to develop bone graft replacements that can repair bone defects without the need for allografts or autografts [1]. With this approach, the porous scaffold serves an important role in the manipulation of the functions of osteoblasts and a central role in the guidance of new bone formation into desired shapes. On the other hand, a sharp rise in musculoskeletal diseases and disorders often demands a drug treatment at the specific defect site [2,3]. Local drug delivery systems are alternative tools in modern medicine because they can assure the optimal level of the drug for longer periods of time and the reduction in possible undesirable side effects. In bone tissue engineering, the term "drug" refers to therapeutic agents such as antibiotics, anti-cancers or anti-inflammatories [4,5]. The potential scaffold as a drug carrier must have the ability to incorporate a drug either physically or chemically, retain the drug at the defect site, and deliver the drug in a controlled manner over time [6–8]. This procedure can simplify treatment for the patient as surgery and drug delivery that combined into one procedure rather than requiring post-surgical systemic and oral administration.

E-mail addresses: samaneh.saber@gmail.com (S. Saber-Samandari), saeedss@aut.ac.ir (S. Saber-Samandari).

In recent years, chitosan and its applications in the field of tissue engineering have attracted considerable attention [9,10]. It has been studied as a useful biomaterial in diverse tissue engineering applications because of its hydrophilic surface that promotes cell adhesion, proliferation and differentiation, good biocompatibility and host response, biodegradability by lysozyme and other enzymes, bactericidal/ bacteriostatic activity, and the capacity to maintain a predefined shape after cross-linking [11–14]. However, chitosan is fragile and does not have enough mechanical properties suitable for bone tissue engineering. The principal advantage of synthetic materials is that their porosity, mechanical strength, and degradation rate can be easily tuned by varying the structures of the polymer and/or the cross-linker. An example of that is poly(acrylic acid), which is a known biocompatible anionic polymer that has been used as a Food and Drug Administration (FDA) approved basic component of a bone cement implant [15]. Another example is polyacrylamide, which is also a synthesized polymer made of a reactive acrylamide monomer [16]. Although the toxicity of the acrylamide monomer has been documented, polyacrylamide is widely used in biomedical applications and drug delivery [17,18]. The mechanical properties of the mentioned polymers still need to be improved which can be achieved by forming a composite of polymer-ceramic materials [19]. Hydroxyapatite (HAp) is one such ceramic, which is a natural mineral constituent of human bone and teeth [20,21]. Biocompatibility, excellent bioactivity and osteoconductivity, being

^{*} Corresponding authors.

non-toxic and non-inflammatory, and excellent chemical and biological affinity with bony tissue of HAp are some of the reasons that HAp is increasingly being explored as bone substitute and drug delivery systems for numerous applications in nano-medicine, orthopedics, and dentistry [4,22,23]. To our knowledge, experimental investigations concerning the composition and synthesis of chitosan-*graft*-poly(acrylic acid-*co*-acrylamide)/n-HAp scaffold as a bone substitute with drug carrier potential have not yet been undertaken.

The aim of the present study is to not only introduce a novel nanocomposite scaffold as a bone substitute, but also reduce the risk of implant failures with anti-inflammatory drug delivery potential. To this end, novel composite scaffolds containing chitosan-graft-poly(acrylic acid-co-acrylamide)/n-HAp using a freeze-drying method were introduced. These scaffolds were characterized by Fourier transform infrared spectroscopy (FTIR), X-ray diffraction analysis (XRD), scanning electron microscopy (SEM), and energy-dispersive X-ray spectroscopy (EDS). Prior to the estimation of drug delivery, the evaluation and verification of their biocompatibility and non-toxicity in the presence of HUGU fibroblastic cells were examined. Drug loading and releasing characteristics of the prepared nanocomposite scaffolds and their kinetics of release were investigated using celecoxib as a model drug. Celecoxib is a selective COX-2 inhibitor drug and is the only non-steroidal antiinflammatory drug (NSAID) that has been approved by the FDA for adjuvant treatment of patients with familial adenomatous polyposis to date [24–27]. Celecoxib has also been shown to inhibit the surviving protein expression in human cancer cells [28–30]. We hypothesized that the celecoxib-loaded scaffold could provide a novel and effective drug carrier to bone healing.

2. Materials and methods

2.1. Materials preparation

Chitosan (average molecular weight, 300,000 g·mol $^{-1}$ and degree of deacetylation (DD), 95%, Aldrich) was dissolved in a dilute solution of acetic acid (Merck). Acrylamide (Merck) and acrylic acid (Merck) were used as monomers, and N_iN^i -methylene-bis-acrylamide (Aldrich) and glutaraldehyde (25% in H_2O , Aldrich) were crosslinkers. Celecoxib as a model drug was extracted from a commercial pill (Celexib® 200, DarouPakhsh Pharmaceutical Mfg. Co. Iran). Nano-HAp was prepared using disodium hydrogen orthophosphate (Analar) and calcium chloride (Aldrich). Sodium hydroxide (Aldrich), sodium chloride (Merck), potassium chloride (Merck), disodium hydrogen phosphate (Merck), potassium dihydrogen phosphate (Merck) and ethanol (Merck) were used as received.

2.2. Synthesis of nano-hydroxyapatite (n-HAp)

In this study, the n-HAP was synthesized through a micro-emulsion technique [31]. A calcium chloride solution (2 mol·L⁻¹) was prepared in a three-necked flask, connected to nitrogen gas, and the temperature was increased to 65 °C. Then, 100 mL of disodium hydrogen phosphate (1.2 mol·L⁻¹) solution was added drop by drop to the calcium chloride solution at a rate of 2 mL· min⁻¹ while stirring vigorously. The pH of the

solution during the reaction of calcium chloride with disodium hydrogen phosphate decreased due to the preparation of hydrochloric acid (see reaction (1)). Therefore, the pH was controlled at 10 ± 0.5 by the addition of a sodium hydroxide solution (1 mol·L $^{-1}$). The product was filtered and washed several times with distilled water and dried overnight in an oven at 60 °C. Thus, n-HAp was formed through the following reaction:

$$10CaCl_2 + 6Na_2HPO_4 + 2H_2O \rightarrow Ca_{10}(PO_4)_6(OH)_2 + 12NaCl + 8HCl$$
 (1)

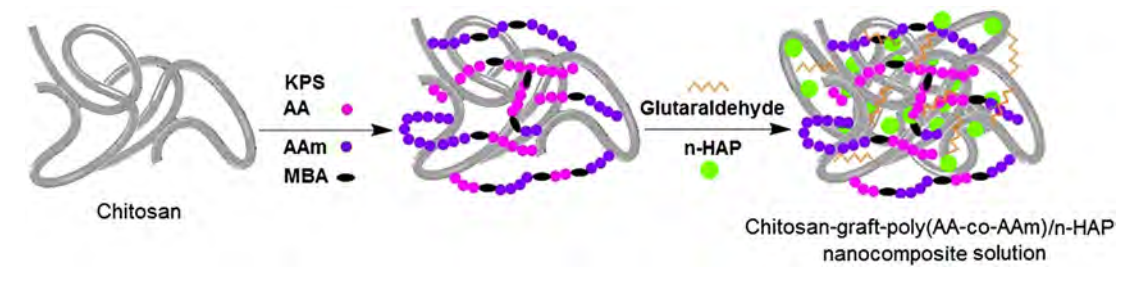
2.3. Fabrication of copolymer grafted chitosan nanocomposite scaffolds

The chitosan-*graft*-poly(acrylic acid-co-acrylamide)/n-HAP nanocomposite scaffolds were synthesized using the following three steps: (I) the preparation of acrylic acid-co-acrylamide (AA-co-AAm)/HAP copolymer grafted chitosan nanocomposite solution; (II) the freezedrying of the solution and the washing, filtering, and dissolving of nanocomposite powder in a suitable solvent; and (III) the freeze-drying of a molded nanocomposite solution and the preparation of scaffolds.

First, a chitosan solution (1.6% W/V) was prepared by dissolving chitosan powder in diluted acetic acid solution (2% V/V) in a two-necked round-bottom flask fitted with a nitrogen gas inlet in a water bath at 60 °C with continuous stirring. Second, the initiator, potassium persulfate (0.04 g), was added to the chitosan solution. After 15 min, acrylic acid (0.25 mL), acrylamide (0.25 mg) and N,N'-methylene-bis-acrylamide (0.04%) were introduced into the above solution in the flask as monomers and a crosslinker, respectively. After stirring the mixture for 30 min, the different amounts of n-HAp powder and glutaraldehyde (25 wt%) were added to the solution, which was then stirred vigorously for 3 h. Finally, the graft polymerization and crosslinking was stopped by cooling the solution and removing the nitrogen gas flow before reaching the gelation point. As shown in Scheme 1, the product of Step 1 was named as the nanocomposite solution, and it was used in the synthesis of the nanocomposite scaffolds. By employing this method, different nanocomposites with different weight ratios of chitosan/ n-HAp 100:0, 100:25, 100:50, and 100:75 were synthesized and named S-0, S-1, S-2, and S-3, respectively.

In Step II, the prepared nanocomposite solution was transferred into a freeze-dryer (FD-10, Pishtaz Engineering Co., Iran) for 48 days. The obtained nanocomposite powder was dispersed in a large volume of distilled water several times to dissolve and remove the remaining unreacted monomers, potassium persulfate, and N,N'-methylene-bisacrylamide. After that, the vacuum-filtered powder was dried in an oven at 50 °C overnight. Finally, the nanocomposite powder was dissolved in a solution of diluted acetic acid (10%) at room temperature with vigorous stirring overnight.

For the synthesis of the grafted nanocomposite scaffold in Step III, the crosslinked chitosan-*graft*-poly(AA-co-AAm) solution containing HAp, which was prepared in Step II was cast into an aluminum mold and transferred to a freezer at $-20\,^{\circ}\text{C}$ for 24 h. The solidified mixture was then placed in a lyophilizer and faced three phases: (I) freezing up to $-70\,^{\circ}\text{C}$ (vacuum 6.4 mbar) for 24 h; (II) warming to $-15\,^{\circ}\text{C}$



Scheme 1. The schematic illustration of the synthesis of chitosan-graft-poly(AA-co-AAm)/n-HAp nanocomposite.

(vacuum 1.4 mbar) for 8 h; and (III) exposure to 30 $^{\circ}$ C (vacuum 0.98 mbar) in the main drying phase for 2 days.

2.4. Characterization of the raw materials and nanocomposite scaffolds

The major phases of chitosan, the prepared n-HAP, and the components of the scaffolds were analyzed using an X-ray diffractometer (Equinox 300) using Cu-K α radiation (1.54 Å) at a 2 θ range of 10–80 $^{\circ}$ with voltage and current settings of 40 kV and 30 mA, respectively. The size of the n-HAp was measured by dynamic light scattering (DLS) using a Malvern Zetasizer NanoZS 3600 (Malvern Instruments Limited, UK). The morphological study and the chemical composition of the scaffolds were performed using scanning electron microscopy (SEM-EDS, Tescan Vega 3 LMU with Bruker Quantax EDS, Czech Republic). Samples were first coated with a thin layer of gold (Au) by a sputtering apparatus. The Brunauer-Emmett-Teller (BET) specific surface areas and Barrett-Joyner Halenda (BJH) pore size distribution were evaluated by adsorption-desorption of nitrogen at liquid nitrogen temperature, using series BEL SORP 18, at 77 K. The chemical structure of chitosan powder and the prepared nanocomposite powder was evaluated using a Fourier Transform Infrared (FTIR) spectroscopy (Perkin-Elmer 400 spectrometer, Llantrisant, UK) over the range of 500-4000 cm⁻¹. Finally, the mechanical properties of the prepared nanocomposite scaffolds with approximately 10 mm in length and 5 mm in diameter were evaluated using a SANTAM (STM-20, Iran) compression test apparatus with 0.5 mm/min. At least three specimens were tested for each sample. The compressive strength and the elastic modulus were the maximum point and the slope of the initial linear portion of the stress-strain curve, respectively.

2.5. Porosity (%) measurements

A liquid displacement method was applied to determine the porosity (%) of synthesized scaffolds [32]. First, a graduated cylinder was filled with a known volume (called V_1) of ethanol and then the dried scaffold was immersed in ethanol. The new volume of the cylinder after immersion of the scaffold was called V_2 . Ethanol was entered and filled pores of the scaffold. Second, the scaffold was removed from the cylinder and the new volume of ethanol in the cylinder was recorded as V_3 . Finally, the porosity (%) of the prepared scaffolds was calculated using the following equation:

porosity (%) =
$$\frac{V_1 - V_3}{V_2 - V_3} \times 100$$
 (2)

2.6. Cell culture and cytotoxicity assay

Human gum fibroblast cells (HUGU) were established taken from the gums of a 45-year old female in the Iranian Biological Resources Center (IBRC). The cell were cultured in a fresh growth medium containing 89% high-glucose Dulbecco's Modified Eagle's Medium (DMEM), 2 mmol· L^{-1} L-glutamine (Biochrom), 10% fetal bovine serum (FBS), and 1% penicillin (Merck). The cells were maintained in a 5% CO₂ humidified incubator at 37 °C and fed every 3 days.

The 3-(4,5-dimethylthiazol-2-yl)-2,5-diphenyltetrazolium-bromide (MTT, Aldrich) assay, which was based on the extraction method, was applied to evaluate the cytotoxic effect of the prepared scaffolds. For this purpose, the HUGU cells were placed into a 96-well culture plate (at a density of 5×10^3 cells in 100 μL of medium per well) in triplicate. The plate was left undisturbed to allow cell attachment to occur. After seeding of the fibroblast cells, they were treated with seven different concentrations of scaffolds (S-1 and S-3) extract (0.03–2.00 mg $\,\text{mL}^{-1}$) and were incubated. After different incubation times (24, 48 and 72 h) and the aspiration of the medium, 20 μL of MTT solution (5 mg $\,\text{mL}^{-1}$ of PBS) was added to each well, including

controls (cells seeded without the addition of the scaffolds extract) and were incubated for another 4 h at 37 °C. The supernatants of wells were then aspirated carefully and formazan precipitate was solubilized with 200 µL of dimethyl sulfoxide (DMSO). Finally, the plate cover was removed and the optical density values were recorded at 570 nm by the absorbance microplate reader (Bio-Tek, ELx-800, USA). Cell viability was calculated according the following equation [12]:

$$Viability~(\%) = \frac{OD_s}{OD_c} \times 100 \eqno(3)$$

where OD_C is the average optical density of the control group and OD_S is the average optical density of each sample.

2.7. Loading and in-vitro release of celecoxib

2.7.1. Extraction of celecoxib from commercial pill

Celecoxib is an NSAID and a poorly water-soluble drug that exhibits anti-inflammatory, analgesic, and antipyretic activities [33]. It was extracted from Celexib® 200 capsules. First, five capsules were opened and their contents were crushed using an agate mortar and pestle to make a fine powder. Second, the powders were transferred to a beaker containing water and were stirred vigorously at room temperature. The solution was filtered and the solids that collected above the filter paper, which contained the water insoluble celecoxib, were dissolved in ethanol and stirred for 30 min. Finally, the solution was filtered and the solvent of the filtrate was stripped from the celecoxib by the evaporation of ethanol in a water bath at 60 °C. Celecoxib with appropriate level of purity was prepared by recrystallization from the ethanol at a low temperature.

2.7.2. Loading of celecoxib

To prepare the celecoxib-loaded nanocomposite scaffolds, the prepared samples (7 mm \times 5 mm with 1.4 g) were first immersed in 30 mL of ethanol and stirred for 30 min. Then, the extracted celecoxib, which was dissolved in 70 mL of ethanol, was added to the above container and maintained under stirring at room temperature. The concentration of the celecoxib solution in the container was $100 \, \mu g \cdot m L^{-1}$. To ensure complete drug loading at specific time intervals, 2 mL of solution was taken, which contained a residual amount of celecoxib and diluted 10 times, and assayed for drug content by a UV–Vis spectrometer (T80 + UV/Vis Spectrophotometer, Beijing PG Instrument Co. Ltd. China) at a wavelength of 254 nm. An identical volume of fresh ethanol was added back into the container after each removal. All samples were measured in triplicate, and a 3% variation was observed in all cases. Finally, the drug loading capacity (DL %) and encapsulation efficiency (EE %) was calculated according to following equation:

Encapsulation efficiency (%) =
$$\frac{C_0V_0 - C_tV_t}{C_0V_0} \times 100$$
 (5)

where, C_0 and C_t are the concentration of the celecoxib solution before and after the scaffold immersion, respectively. V_0 and V_t are the volume of the celecoxib solution before and after the scaffold immersion, and W is the weight of the scaffold (carrier).

2.7.3. In vitro release of celecoxib

To monitor the release of celecoxib, the drug-loaded nanocomposite scaffolds were suspended in PBS (pH 7.4) and stirred continuously at 37 °C. The PBS solution was prepared by dissolving sodium chloride (4.0 g), potassium chloride (0.1 g), disodium hydrogen phosphate (0.72 g) and potassium dihydrogen phosphate (0.12 g) in 400 mL of water. The pH was then adjusted to 7.4 using hydrochloric acid

 $(0.1 \text{ mol} \cdot \text{L}^{-1})$, and the total volume reached 500 mL by the addition of extra bi-distilled water.

The amount of the released celecoxib was determined by studying the aliquots of the release medium at predetermined time intervals. The same volume of fresh solution was added to the container to keep the volume of the solution constant (250 mL). The amount of celecoxib released at each time point was determined by a UV–Vis spectrometer, as described above. The cumulative celecoxib release was calculated using the following equation:

$$\label{eq:cumulative drug relaese} \text{Cumulative drug relaese} \ (\%) = \frac{C_r V_r}{C_0 V_0 - C_t V_t} \times 100 \eqno(6)$$

where C_r and V_r are the concentration and volume of the solution after release of celecoxib. In addition, $C_0V_0-C_tV_t$ is the weight of the loaded celecoxib in the scaffold.

2.7.4. Kinetic of celecoxib release

To investigate the mechanism of drug release and to determine the release efficiency, five kinetic models were studied: zero-order, first-order, Higuchi, Ritger-Peppas, and Kopcha. Zero order describes systems in which the drug release rate is independent of the concentration of the loaded drugs (Fickian), whereas the first order model is for systems with concentration-dependent release rates (non-Fickian). Ritger-Peppas developed an empirical equation to analyze both the Fickian and the non-Fickian release of drugs [34]. Higuchi is a classical model

to study the release of a drug incorporated in an insoluble polymeric matrix. Throughout the study, the Kopcha model proved that the release process was dominated by diffusion or erosion. These models are given in the following equations:

$$Q_t = Q_0 + K_0 t \tag{7}$$

$$Log(Q_0 - Q_t) = \frac{K_1 t}{2.303} \tag{8}$$

$$Q_t = K_H t^{1/2} \tag{9}$$

$$\frac{Q_t}{Q_{tr}} = K_P t^n \tag{10}$$

$$\frac{Q_t}{t} = \frac{A}{t^{1/2}} + B \tag{11} \label{eq:11}$$

In these equations, t is the time, Q_0 is the initial concentration of drug and Q_t is the amount of drug released at time t. Q_t/Q_∞ is the fraction of drug release at time t. k is the release rate constant. In the Kopcha equation, A and B are the relative contributions of diffusion and erosion, respectively.

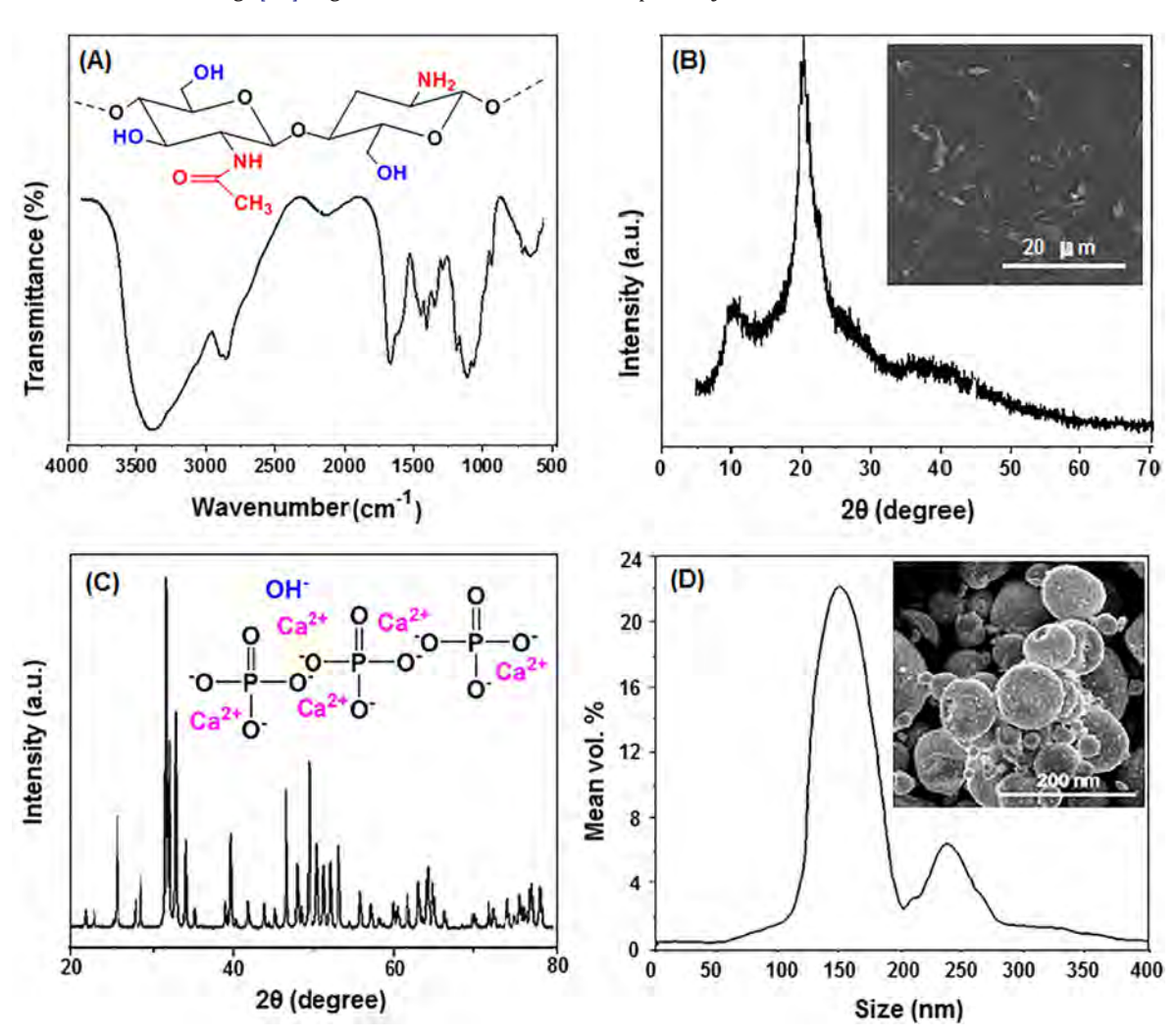


Fig. 1. (A) FTIR spectrum of chitosan powder and (B) X-ray diffractograms. The inserts show the chemical structure of chitosan powder and the SEM image. (C) X-ray diffractograms and (D) size distribution of the synthesized nano-HAp powder. The inserts show chemical structure and the SEM image of the synthesized nano-HAp powder.

3. Results and discussion

3.1. Characterization of the raw materials

The FTIR spectrum of chitosan is shown in Fig. 1A. The most typical absorption bands of chitosan situated at 1597 cm⁻¹ related to the amine in the deacetylated rings of chitosan and at 1655 cm⁻¹, they correspond to the amide I bands in the acetylated rings of chitosan [35]. The C—H and O—H bending vibrations in the chitosan spectrum were observed between 1300 cm⁻¹ and 1400 cm⁻¹ with a sharp peak at 1383 cm⁻¹ attributed to the O—H bending vibration. Furthermore, the two intensive peaks at 1159 cm⁻¹ and 1082 cm⁻¹ correspond to the anti-symmetric stretching of the C—O—C bridge and the skeletal vibrations involving the C—O stretching, respectively. The peaks are generally regarded as the finger print peaks for the saccharide structure of chitosan [36]. Moreover, the peaks assigned to the C—O stretching vibrations of the chitosan rings were located in the 1000–1300 cm⁻¹ region.

The XRD spectrum for chitosan is presented in Fig. 1B. The X-ray pattern of chitosan revealed two characteristic broad diffraction peaks at 20 of 10° and 20°, which are typical fingerprints of semicrystalline chitosan. It is obvious that chitosan is a crystal polymer to some degree, which suggests the formation of inter- and intra-molecular hydrogen bonds in the presence of free amino groups in chitosan [37]. In addition, the morphology of chitosan was examined using SEM (the insert in Fig. 1B). The figure shows that the chitosan exhibited a smooth surface with several white spots visible on the image, which are probably due to impurities and dust particles.

A typical XRD profile of HAp nanoparticles is shown in Fig. 1C. The XRD phase analysis was in good agreement with the reported result by Zanotto et al. [38]. According to their findings, the XRD pattern of HAp could be described by a hexagonal HAp phase. For example, the existence of 2θ peaks at approximately 23.2° , 26° , 29.3° , 32.2° , 46.6° , and

49.4° correspond to the diffraction planes (211), (002), (210), (300), (222) and (213) of the HAp crystallites, respectively. These data confirmed the major phase as HAp particles. DLS measurement (Fig. 1D) showed the nanometer-scale dimensions of the particles, with a bimodal size distribution centered approximately at 150 nm and 230 nm, and mean volumes of 22% and 6%, respectively. The SEM observations of n-HAp (insert in Fig. 1D) confirmed the results of the DLS analysis. Spherical-shaped particles with clumped distributions were visible from the SEM analysis. These figures show the addition of polydisperse and heterogeneous mixtures of n-HAp addition to the spherical morphology. The mean diameters varied from approximately 20 nm to 250 nm.

3.2. Characterization of the copolymer grafted chitosan nanocomposite scaffolds

3.2.1. Fourier transform infrared (FTIR) analysis

FTIR spectral analyses were performed to confirm the grafting of AA-co-AAm onto chitosan and the presence of HAp in the structure of the nanocomposite scaffolds. The most typical absorption bands of chitosan appeared at 1597 cm⁻¹ and 1605 cm⁻¹, which are extensively explained in Section 3.1 had a minor shift and obtained at 1605 cm⁻¹ and 1658 cm⁻¹ in the spectra of all samples. The modifications that took place during the grafting of AA-co-AAm to chitosan can be confirmed by the presence of the aforementioned intensive peaks and can be attributed to the overlapping of amine and amide vibration peaks of chitosan with the vibration of the C=O (in acrylamide and acrylic acid) and N—H bonds (in acrylamide). The intensity of these bands decreased in the spectra of S-0 to S-3, which indicated that the functional groups of the monomers and the N—H groups of chitosan took part in the bonding with n-HAp. In addition, the peak at 1406 cm⁻¹ in the nanocomposite scaffolds spectra, especially the S-O sample, related to C-N stretching can

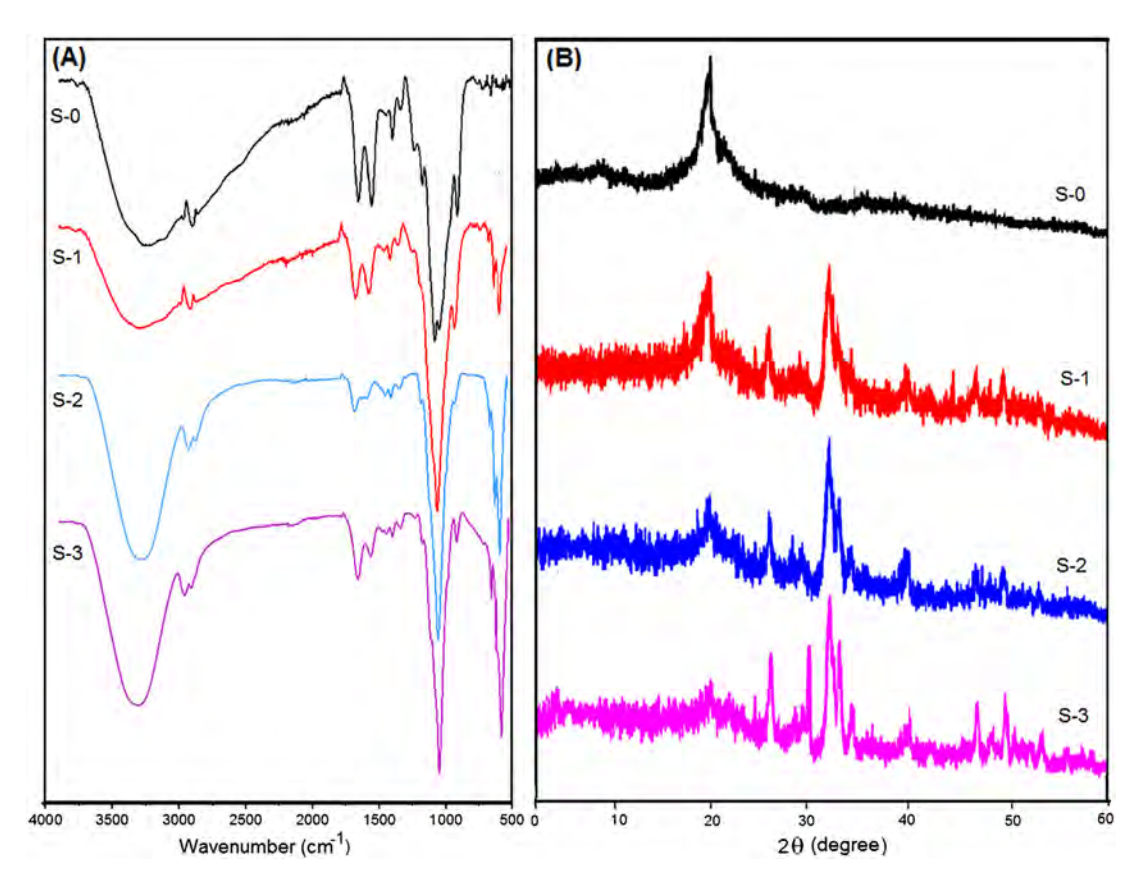


Fig. 2. (A) FTIR spectra and (B) X-ray diffractograms of the prepared nanocomposite scaffolds.

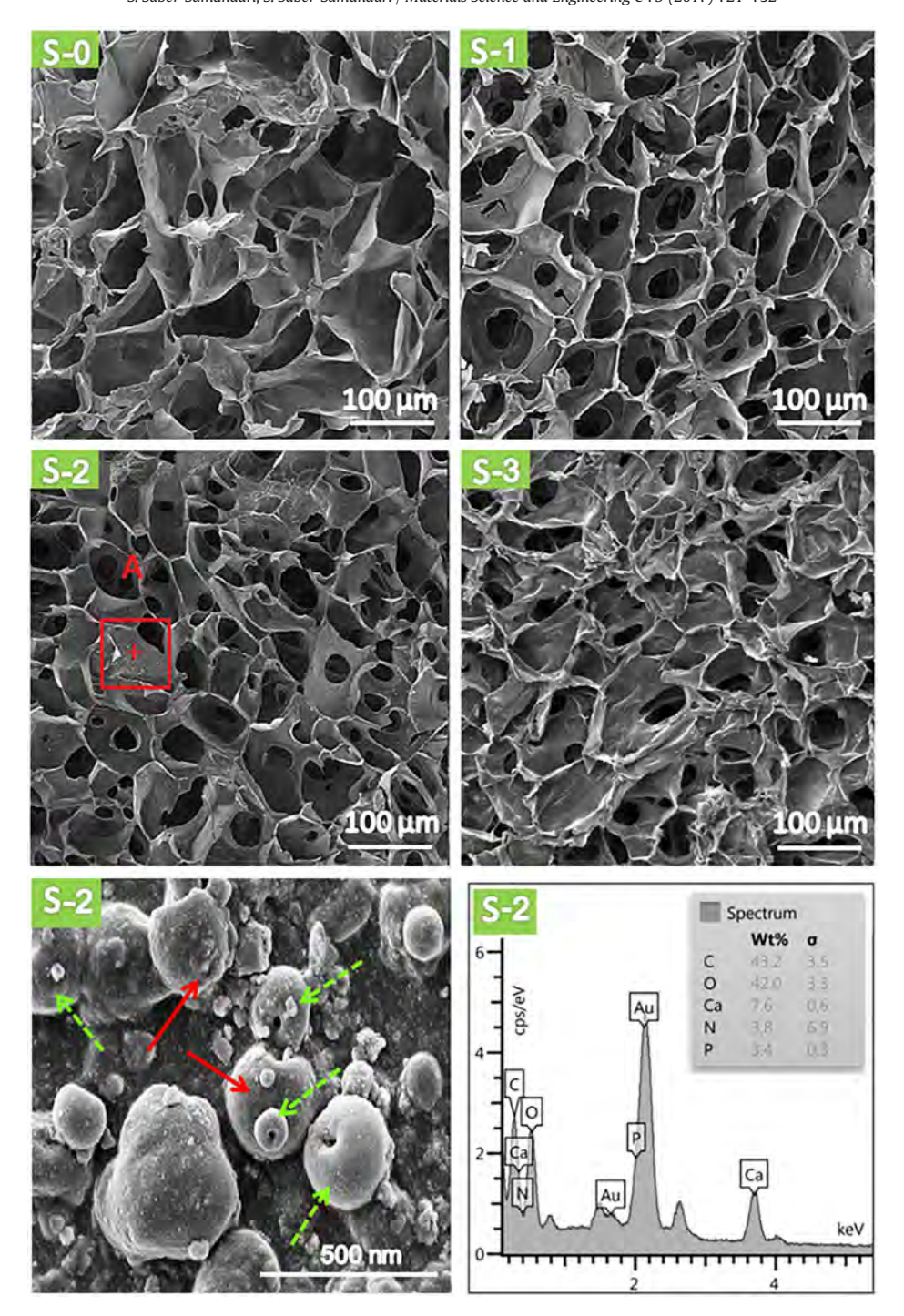


Fig. 3. The SEM images of the nanocomposite scaffolds. The solid (red) arrows in the high magnification SEM image for S-2 sample indicate copolymer grafted to chitosan and dashed (green) arrows indicate HAp nano-particles. EDS point analysis for elemental composition of the prepared nanocomposite scaffold (S-2). (For interpretation of the references to color in this figure legend, the reader is referred to the web version of this article.)

support the grafting of AA-co-AAm onto chitosan [39]. The peak at 2924 cm⁻¹ was attributed to the sp³ C—H stretching vibration of the chitosan backbone and poly(AA-co-AAm) grafted chitosan. As seen in Fig. 2A, the broad absorption peak between 3000 cm⁻¹ and 3700 cm⁻¹ was assigned to the stretching vibration of the hydroxyl groups of chitosan, HAp and/or the presence of water, which overlapped with the —NH₂ stretching vibration peak of chitosan. The intensity of the mentioned peak increased and became sharper after increasing the amount of HAp from S-0 to S-3. The absorption bands of HAp were located at 1029 cm⁻¹, 1092 cm⁻¹, and 961 cm⁻¹, corresponding to symmetric and asymmetric stretching

Table 1Mechanical properties of the synthesized copolymer grafted nanocomposite scaffolds and human hone

Sample	Compressive strength (MPa)	Elastic modulus (GPa)			
S-0	0.13 ± 0.5	0.01 + 0.3			
S-1	2.15 ± 0.2	0.33 ± 0.1			
S-2	2.79 ± 0.2	0.41 ± 0.1			
S-3	3.58 ± 0.3	0.57 ± 0.2			
Trabecular bone ^a	5.30	0.44			

a [45].

Table 2Pore size and porosity of the synthesized copolymer grafted nanocomposite scaffolds.

Sample	Pore size ^a (μm)	Porosity ^b (%)	Surface area ^c (m ² ·g ⁻¹)	Pore size ^d (nm)
S-0	122 ± 4	21 ± 0.4	_	-
S-1	108 ± 3	54 ± 0.9	10.8	148
S-2	96 ± 5	61 ± 0.1	_	-
S-3	75 ± 5	72 ± 0.5	55.1	47

Obtained from

- ^a ImageJ software.
- b Liquid displacement method.
- c BET analysis.
- d BJH analysis.

modes of PO_4^{3-} in HAp, respectively. Finally, regarding the spectrum of chitosan-graft-poly(AA-co-AAm) (S-0) and the nanocomposite scaffolds (S-1 to S-3), the intensity of the absorption bands at 602 and 566 cm⁻¹ was attributed to the symmetric stretching and bending modes of the O—P—O bonds of the phosphate groups in HAp were improved by increasing the HAp contents in the nanocomposite scaffolds (from S-1 to S-3). These results confirmed the synthesis of chitosan-graft-poly(AA-co-AAm)/n-HAp nanocomposite scaffolds.

3.2.2. X-ray diffraction (XRD) analysis

Fig. 2B shows the X-ray diffractograms of the synthesized nanocomposite scaffolds, According to the XRD pattern of chitosan (Fig. 1B) compared to the nanocomposite scaffolds (Fig. 2B) especially S-0 sample, the first peak at 2θ of 10° disappeared and the second peak at 20° appeared less intense in all the prepared nanocomposite scaffolds. This reduction in crystallinity could be attributed to the formation of bonds between monomers AA-co-AAm and chitosan during grafting process. This can lead to more disordering in the crystalline region of chitosan with a concomitant increase in the amorphous region. These supportive results also confirmed the grafting of poly(AA-co-AAm) onto chitosan through the synthesis of the nanocomposite scaffolds. In addition, for all samples of S-1 to S-3, peaks at approximately 23°, 26°, 29°, 32°, 46°, and 49°were observed and are related to the HAp crystallites. These peaks are in good accordance with the peaks observed in Fig. 1C, which confirmed the presence of n-HAp in the scaffold structure. According to that, it was obvious that the intensity of the mentioned peaks was increased by increasing the amount of n-HAp. In addition, the intensity of the peak at $2\theta = 20^{\circ}$, which was assigned to the (100) reflection of orthorhombic (form II) crystal of chitosan, was decreased by increasing the amount of n-HAp (samples S-1 to S-3) due to the strong ionic interactions between n-HAp and chitosan. This result is consistent with the previous observations obtained from the FTIR

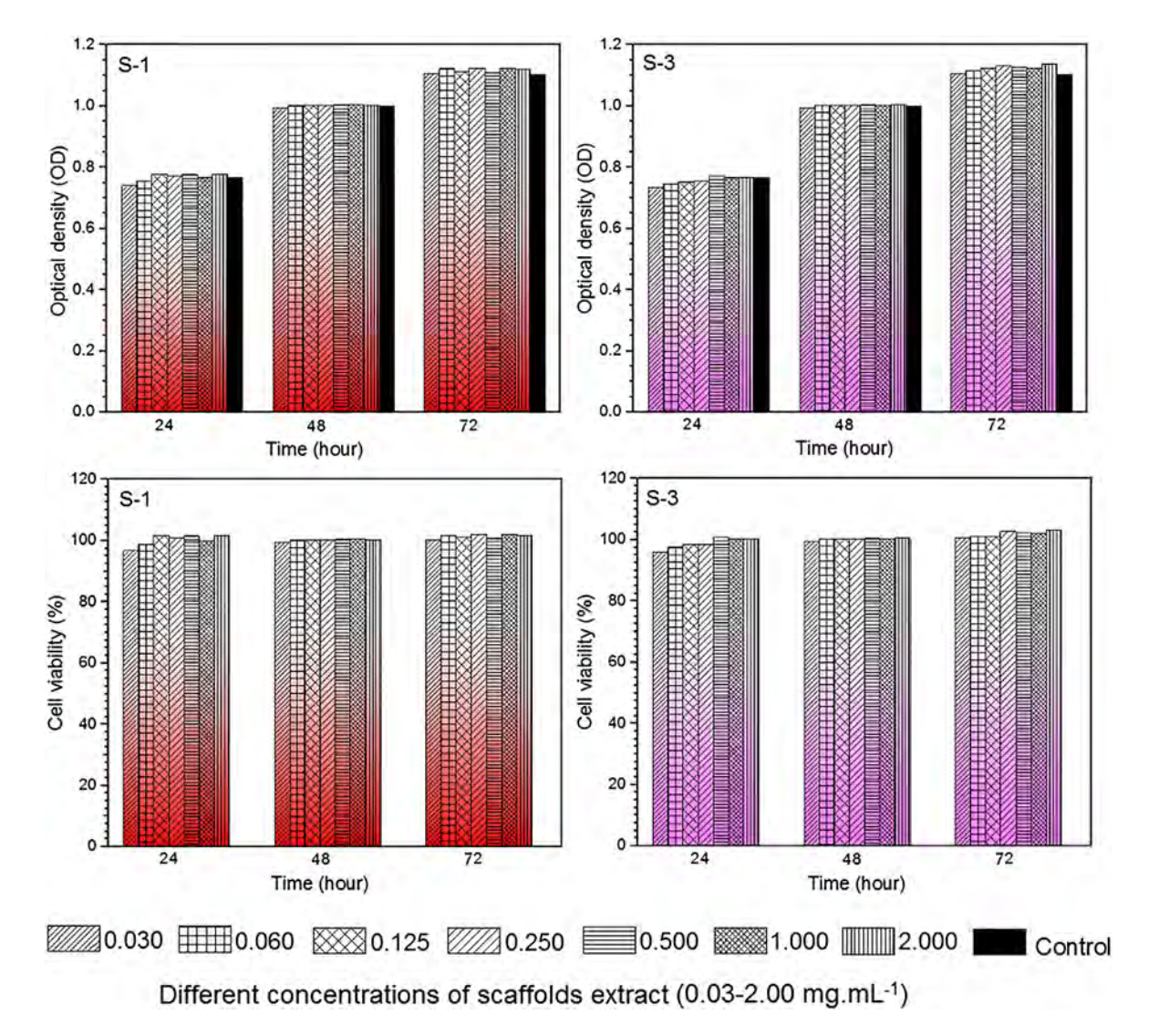


Fig. 4. MTT assay of HUGU cells for the scaffolds (S-1 and S-3) extracts (0.03-2.0 mg·mL⁻¹) in terms of optical density values and the normalized cell viability (%) after 24, 48, and 72 h.

analysis and the scheme of synthesis procedure of the nanocomposite scaffold.

3.2.3. Scanning electron microscopy (SEM) analysis

Fig. 3 shows the microstructures of the nanocomposite scaffold components, which contains several irregular pores connected to each other with the walls of chitosan-*graft*-poly(acrylic acid-*co*-acrylamide)/HAp nanocomposites. In addition, the spherical particles of n-HAp (<200 nm) in the high magnification SEM image of samples S-2 have been shown (green arrows).

The EDS of the S-2 nanocomposite scaffold in Fig. 3 displays the main signals for AA (i.e., carbon, and oxygen), n-HAp (i.e., calcium, phosphorus, and oxygen) and AAm and chitosan (i.e., carbon, oxygen and nitrogen). By selecting the random place in the wall of pores and according to the EDS spectrum, it can be concluded that the mentioned elements of applied materials over the entire nanocomposites homogeneously distributed within the scaffolds.

3.2.4. Mechanical properties of the prepared scaffolds

The elastic modulus and compressive strength of the prepared scaffolds are listed in Table 1. As shown in Table 1, the mechanical properties of the prepared scaffolds are particularly satisfactory and the obtained mechanical values are in the range reported for trabecular bone (i.e., 2–6 MPa compressive strength and 0.1–0.3 GPa an elastic

modulus), which has 75–85% porosity with pores 300–600 µm in diameter [40]. In addition, the table shows that the compressive strength (from 0.13 \pm 0.5 to 3.58 \pm 0.3) and the elastic modulus (from 0.01 \pm 0.3 to 0.57 \pm 0.2) of nanocomposite scaffolds were improved in samples S-0 to S-3 due to the increasing the HAp amount in the structure of the scaffolds. This can be attributed to the high crystallinity of HAp [41] and higher elastic modulus of the HAp (i.e., 18 \pm 5 GPa [42]) compared with polyacrylamide (i.e., 30 \pm 10 KPa [43]), and chitosan (i.e., 17.99 \pm 0.11 MPa [44]). Therefore, it is expected that sample S-3 with the highest amounts of n-HAp would have the best mechanical properties.

3.2.5. Porosity of the prepared scaffolds

Porosity measurements were done with ethanol by the liquid displacement method. Ethanol did not cause a change in pore size, therefore used as displacement medium. The results are presented in Table 2. The amounts of HAp nanoparticles directly affect the porosity and average pore size of the scaffolds. Mancini et al. reported that there is a direct relationship between the porosity and the phase of the HAp sample [46]. In fact, porosity increases as the crystallinity increases [47]. Table 2 shows that the porosity increased (from 21 to 72%) by increasing the HAp nanoparticle amounts from S-0 to S-3; consequently, the average pore size decreased from 122 µm to 75 µm due to the increase in crystallinity of the prepared grafted polymer nanocomposite scaffolds. In addition, the scaffolds should have enough space

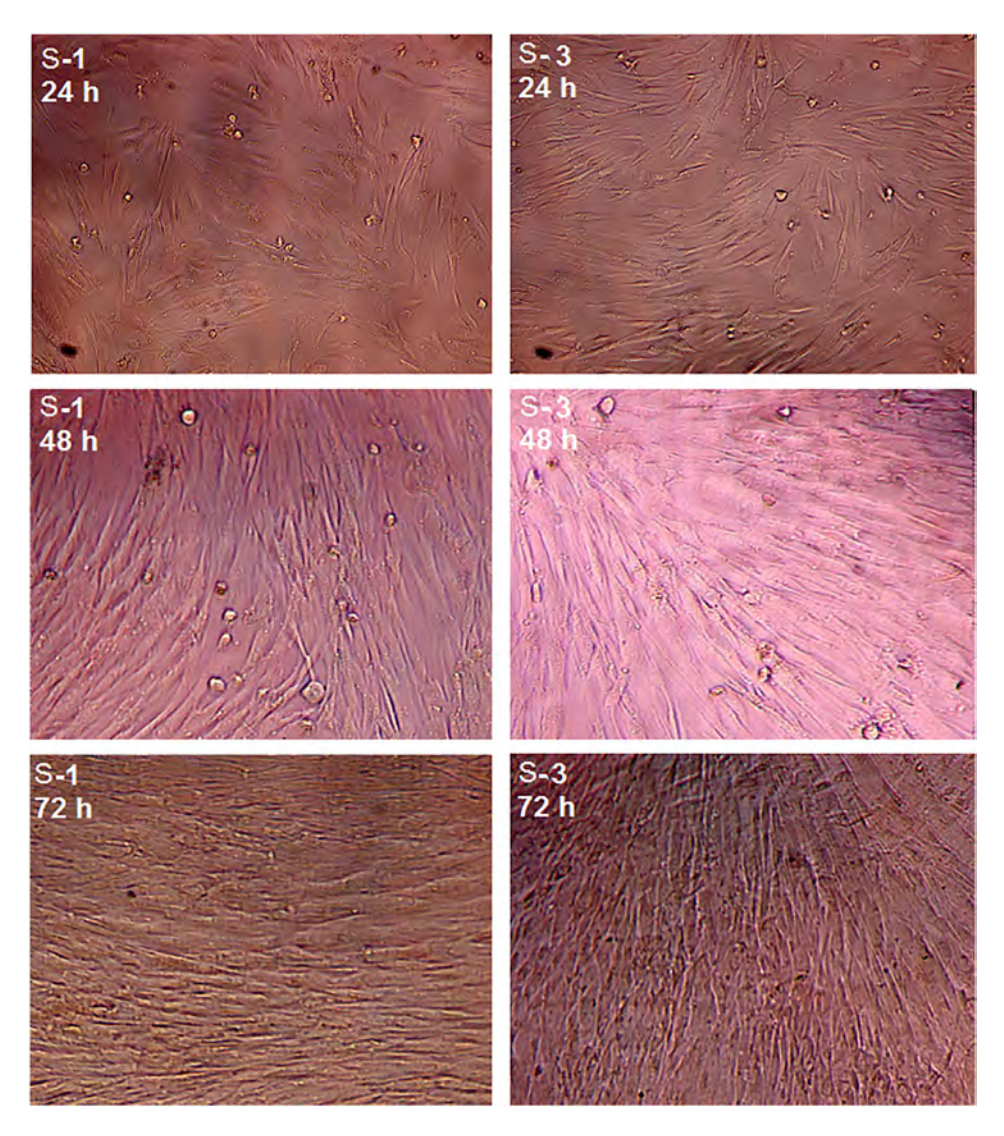
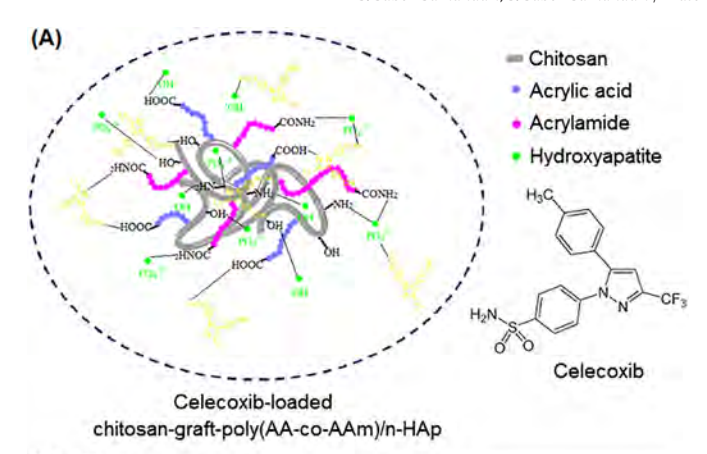


Fig. 5. Optical images of the cell morphology in the presence of the scaffolds (S-1 and S-3) extract after 24, 48, and 72 h.



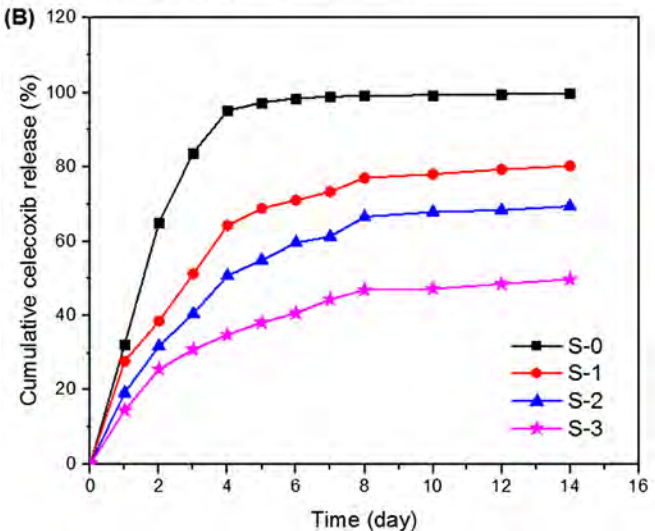


Fig. 6. (A) The schematic illustration for the loading of celecoxib on the prepared nanocomposite and (B) The effect of time on the cumulative drug release (%) from the nanocomposite scaffolds.

for seeding cells, the entering of nutrients, blood vessels and growth factors and exiting of waste size of The pores should be at least a few times bigger than the cell size. Scaffolds with pores in the range of 50–400 μm can promote osteoblast cell growth and proliferation [48]. The results indicated that the presence of HAp nanoparticles caused rougher pore walls and open interconnected pores, which were, respectively, suitable for cell adhesion and promoted native tissue in growth and fluid exchange.

3.3. Brunauer-Emmett-Teller (BET) and Barrett-Joyner Halenda (BJH) analysis

The total surface area and pore size distribution of the prepared scaffolds' (S-1 and S-3) were verified by BET and BJH analysis. The results presented in Table 2, revealed that all the scaffolds contained numerous mesopores; however, the BET surface area for S-3 sample was 55.1 $\rm m^2 \cdot g^{-1}$, which was much higher than the corresponding value

for S-1 scaffolds (10.8 m $^2 \cdot g^{-1}$). BET analysis of adsorption-desorption isotherms, in the presence of a sharp adsorption step in the P/P $_0$ region from 0.9 to 1.00, indicated that the materials processed a well-defined and regular array of mesoporous. Furthermore, the N $_2$ absorption isotherm of samples is a type IV isotherm with a typical H2 hysteresis loop according to then IUPAC classification. Furthermore, the pore-size distribution calculated by the BJH method revealed that the size of mesopores for S-3 scaffold was 47 nm, while that for S-1 sample was 148 nm. This difference in the mesopore size distribution that has been reported is due to the amounts of n-HAp and its interaction chitosan-graft-poly(AA-co-AAm) polymer, which leads to the reduction in the mesopores size.

3.4. Cytotoxicity evaluation of the nanocomposite scaffolds

To apply the prepared scaffolds as a bone implant and carrier of drugs generally for biological applications, it is necessary to consider their cytocompatibility through in vitro assays. The biomaterial cytotoxicity can emanate from the original material itself as well as from the byproducts that may leach out from the material [49]. The cytotoxicity of the prepared scaffolds' (S-1 and S-3) extracts was examined by determining the viability of HUGU cells in comparison with the control. As shown in Fig. 4, scaffolds' extracts (up to 2 mg·mL⁻¹) have good cell viability. The cell viability for both samples' extracts is significantly higher than that of control samples after 72 h culturing, which refers to a higher proliferation rate. In addition, the optical imaging of the HUGU fibroblastic cells in Fig. 5, which shows that the cells are densely arranged and seem to be piled up on each other, confirmed the results of the MTT assay. It can be concluded that the prepared cytocompatible and nontoxic scaffolds with a high proliferation rate can potentially be used in biomedical applications.

3.5. Drug delivery of the prepared scaffolds

3.5.1. In vitro load of celecoxib

Loading capacity and encapsulation efficiency are critical characteristics for evaluating the capacity of a selected carrier to entrap and carry a selected drug. As seen in Fig. 6, celecoxib as a drug was successfully loaded into the prepared nanocomposite scaffolds by ionic interactions. In this study, the synthesized carrier included different functional groups, $-COOH (-COO^{-})$, $-CONH_2 (-O^{-}C=N^{+}H_2)$ and -OH (-0^{-}) , which can undergo hydrogen and ionic bonding with celecoxib. In addition, the presence of HAp in the structure of the prepared nanocomposite scaffolds as a physical crosslinker, containing ionic groups such as PO₄³ and OH⁻, increases the possibility of electrostatic interaction with positively charged celecoxib. Thus, the loading of the drug is expected to increase considerably with an increase in the amount of HAp in the nanocomposite scaffold structure (S-0 to S-3). The results of the LC percentage and EE percentage (shown in Table 3), confirmed the above hypothesis. The maximum LC (63.2%) and EE (97.6%) belonged to the S-3 sample, which had the highest amount of HAp.

3.5.2. In vitro release of celecoxib

The cumulative release of celecoxib from the synthesized nanocomposite scaffolds is shown in Fig. 6. The experimental results of the UV–Vis spectroscopy revealed that the S-0 sample released the maximum

Table 3The encapsulation efficiency and kinetic parameters for release of celecoxib from nanocomposite scaffolds.

Samples	LC (%)	EE (%)	Zero oi	der	First order Higuchi		Ritger-Peppas			Kopcha				
			Ko	R ²	K ₁	R ²	K _H	R ²	n	K _R	R ²	A	В	R ²
S-0	46.5	65.2	5.64	0.5784	-0.093	0.5419	22.88	0.7236	0.2566	31.88	0.7902	43.8	0.06	0.9586
S-1	52.0	72.8	2.17	0.5761	-0.054	0.5147	14.07	0.6794	0.2930	21.87	0.8650	23.7	0.75	0.9802
S-2	57.5	80.5	2.35	0.7663	-0.074	0.6984	12.41	0.9027	0.3636	16.63	0.9408	17.8	1.26	0.9821
S-3	63.2	88.6	1.92	0.8033	-0.076	0.7574	9.818	0.9311	0.3667	13.02	0.9849	14.4	0.20	0.9955

amount of celecoxib (95.2%), with an extremely high release rate compared to the others during the first 4 days. This initial burst release was attributed to the rapid desorption of drug from the surface of the scaffolds. The amount of released drug gradually decreased with a relatively steady release rate until day 14. In addition, with an increase in the amount of HAp, a decrease in the release percentage was observed. Furthermore, the results indicated that 80.3% and 69.5% of the loaded celecoxib was released by the S-1 and S-2 samples after 14 days, respectively. The S-3 sample, with the highest amount of HAp and consequently the highest encapsulation efficiency (88.6%), was able to maintain 48.2% of the loaded celecoxib amount, whereas almost all of the celecoxib was released from the S-0 sample.

The calculated amounts of drug released from the nanocomposite scaffold in the PBS solution at 37 °C were dependent on the composition and the morphology of the scaffold. For example, the ionic interaction and hydrogen bonds between HAp and celecoxib in samples containing different amounts of HAp acted as barriers against the release of the entrapped drug from the nanocomposite scaffolds. In addition, the size of the pores was decreased by increasing the HAp amounts in the composition of S-0 to S-3, which could cause a reduction in drug release.

3.5.3. Kinetic modeling of celecoxib release

The release of the drug from these scaffolds includes: (I) diffusion through the scaffold polymeric matrix; (II) desorption of the surface bound/adsorbed drug; (III) scaffold polymeric matrix erosion; and (IV) a combined erosion/diffusion process [50]. In this survey, five kinetic models (i.e.: zero order, first order, Higuchi, Ritger-Peppas and

Kopcha) were applied, and the experimental drug release data were treated with various kinetic models to find the best fit. The plots of the kinetic models for all samples are shown in Fig. 7, and their parameters, calculated using Eqs. (7)–(11), are given in Table 3. According to Fig. 7 and Table 3, the calculated values of the celecoxib release amount using the Higuchi (Eq. (9)), Ritger-Peppas (Eq. (10)), and Kopcha (Eq. (11)) models especially for samples S-2 and S-3 are in agreement with the experimental cumulative release values in which they have a good correlation coefficient (R²). In the Ritger-Peppas model, the mechanisms of drug release are characterized using the release exponent ("n" value) which indicate the mechanism of drug release from cylindrical carriers to be Fickian ($n \le 0.43$), non-Fickian release or anomalous (0.43 < n < 0.85), and for case II transport, n = 0.85 [34]. Based on the data in Table 3, the value of n for all the samples is <0.43, indicating that drug release was controlled only by Fickian diffusion. In Fickian diffusion, the rate of release is independent of the drug concentration in the carrier. In addition, the Kopcha equation was used to better indicate the release mechanism and to quantify the relative contributions of diffusion (A) and erosion (B) during drug release [51]. The data in Table 3 show that the diffusion coefficient A is far greater than B, suggesting that the drug release from the prepared nanocomposite scaffolds was mainly controlled by a diffusion process. Drug release by diffusion involves three steps. First, the water penetrates into the polymeric system of scaffolds. Second, the conversion of a glassy polymer is converted into a rubbery matrix. Third, the drug from the swollen rubbery matrix is diffused. In addition, the kinetic constants (K_R) were lower when the n-HAp concentration increased (see Table 3), which indicated that the

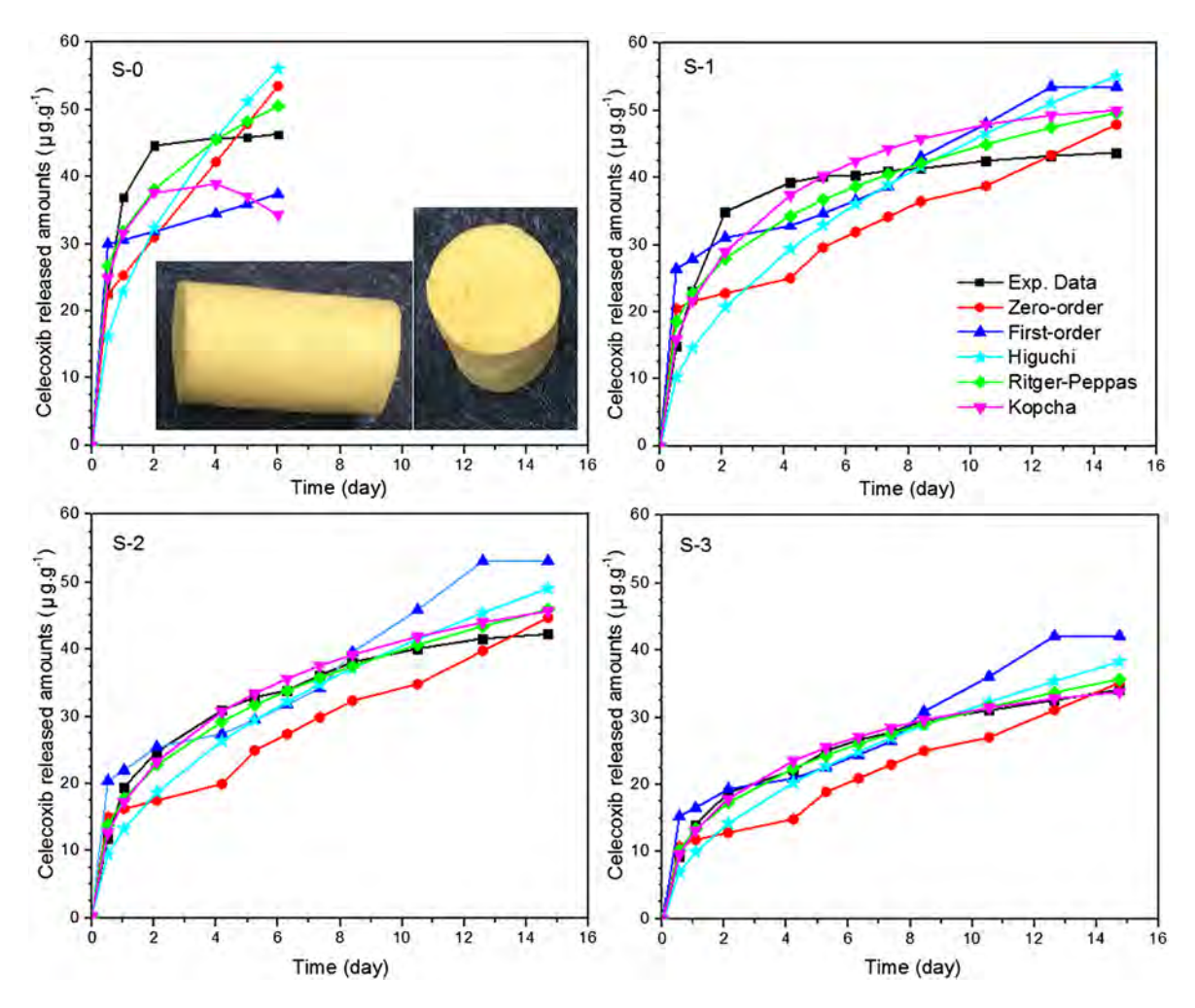


Fig. 7. The kinetics of celecoxib release from the prepared nanocomposite scaffolds by zero order, first order, Higuchi, Ritger-Peppas and Kopcha.

diffusion rate decreased when the n-HAp quantity increased due to the interaction of n-HAp with celecoxib. This issue confirmed our findings concerning the effect of n-HAp on the celecoxib release from scaffolds.

4. Conclusions

In this study, chitosan-graft-poly(AA-co-AAm)/HAp nanocomposite scaffolds were synthesized through a novel multi-step route as a bone implant and a drug carrier. The prepared scaffolds were characterized using FTIR, XRD, SEM and EDX. The presence of grafted copolymer and n-HAp in the structure of the scaffolds was confirmed. We found that mechanical strength of the scaffolds can be improved by either increasing the HAp nanoparticles amounts or reducing pore size of the scaffolds. The cytotoxicity of the prepared scaffolds' extracts was examined by determining the viability of HUGU cells using MTT assays. The results of the cell culture experiments demonstrated that the prepared scaffolds have good cytocompatibility without any cytotoxicity. We also found that increasing amount of the HAp nanoparticles improves cell viability and proliferation on the scaffolds. The presence of the HAp nanoparticles affected the celecoxib (selected model drug) loading and the encapsulation efficiency of the prepared scaffolds. The celecoxib release followed the Higuchi, Ritger-Peppas, and Kopcha kinetic models. Results from the Kopcha models revealed that the release of celecoxib from the prepared nanocomposite scaffolds was mainly controlled by a diffusion process. Thus, these initial studies indicated that the prepared biocompatible nanocomposite scaffolds can be used to in-vivo studies for further assessment in bone tissue engineering.

Appendix A. Supplementary data

Supplementary data to this article can be found online at http://dx.doi.org/10.1016/j.msec.2017.02.112.

References

- S.L. Salkeld, L.P. Patron, R.L. Barrack, S.D. Cook, The effect of osteogenic protein-1 on the healing of segmental bone defects treated with autograft or allograft bone, J. Bone Joint Surg, Am. 83-A (2001) 803–816.
- [2] G.S. Lee, J.H. Park, U.S. Shin, H.W. Kim, Direct deposited porous scaffolds of calcium phosphate cement with alginate for drug delivery and bone tissue engineering, Acta Biomater. 7 (2011) 3178–3186.
- [3] W. Hur, M. Park, J.Y. Lee, M.H. Kim, S.H. Lee, C.G. Park, S.N. Kim, H.S. Min, H.J. Min, J.H. Chai, S.J. Lee, S. Kim, T.H. Choi, Y.B. Choy, Bioabsorbable bone plates enabled with local, sustained delivery of alendronate for bone regeneration, J. Control. Release 222 (2016) 97–106.
- [4] S. Bose, S. Tarafder, Calcium phosphate ceramic systems in growth factor and drug delivery for bone tissue engineering: a review, Acta Biomater. 8 (2012) 1401–1421.
- [5] X.H. Zhou, D.X. Wei, H.M. Ye, X. Zhang, X. Meng, Q. Zhou, Development of poly(vinyl alcohol) porous scaffold with high strength and well ciprofloxacin release efficiency, Mater. Sci. Eng. C 67 (2016) 326–335.
- [6] G. Rijal, W. Li, 3D scaffolds in breast cancer research, Biomaterials 81 (2016) 135–156.
- [7] F.J. Martínez-Vázquez, M.V. Cabañas, J.L. Paris, D. Lozano, M. Vallet-Regí, Fabrication of novel Si-doped hydroxyapatite/gelatine scaffolds by rapid prototyping for drug delivery and bone regeneration, Acta Biomater. 15 (2015) 200–209.
- [8] Z. Fereshteh, M. Fathi, A. Bagri, A.R. Boccaccini, Preparation and characterization of aligned porous PCL/zein scaffolds as drug delivery systems via improved unidirectional freeze-drying method, Mater. Sci. Eng. C 68 (2016) 613–622.
- [9] M. Naeimi, M. Rafienia, M. Fathi, M. Janmaleki, S. Bonakdar, M. Ebrahimian-Hosseinabadi, Incorporation of chitosan nanoparticles into silk fibroin-based porous scaffolds: Chondrogenic differentiation of stem cells, Int. J. Polym. Mater. 65 (2016) 202–209.
- [10] I.M. El-Sherbiny, S. Yahia, M.A. Messiery, F.M. Reicha, Preparation and physicochemical characterization of new nanocomposites based on β-type chitosan and nanohydroxyapatite as potential bone substitute materials, Int. J. Polym. Mater. 63 (2014) 213–220.
- [11] R.A.A. Muzzarelli, V. Ramos, V. Stanic, B. Dubini, M. Mattioli-Belmonte, G. Tosi, R. Giardino, Osteogenesis promoted by calcium phosphate N, N-dicarboxymethyl chitosan, Carbohydr. Polym. 36 (1998) 267–276.
- [12] E. Khor, L.Y. Lim, Implantable applications of chitin and chitosan, Biomaterials 24 (2003) 2339–2349.
- [13] M. Mattioli-Belmonte, G. Biagini, R.A.A. Muzzarelli, C. Castaldini, M.G. Gandolfi, A. Krajewski, A. Ravaglioli, M. Fini, R. Giardino, Osteoinduction in the presence of chitosan-coated porous hydroxyapatite, J. Bioact. Compat. Polym. 10 (1995) 249–257.

- [14] S. Sedaghat, Synthesis and characterization of new biocompatible copolymer: chitosan-graft-polyaniline. Int. Nano Lett. 4 (2014) 1–6.
- [15] N. Rahimi, G. Swennen, S. Verbruggen, M. Scibiorek, D.G. Molin, M.J. Post, Short stimulation of electro-responsive PAA/fibrin hydrogel induces collagen production, Tissue Eng. Part C Methods 20 (2014) 703–713.
- [16] S. Saber-Samandari, S. Saber-Samandari, S. Kiyazar, J. Aghazadeh, A. Sadeghi, In vitro evaluation for apatite-forming ability of cellulose-based nanocomposite scaffolds for bone tissue engineering, Int. J. Biol. Macromol. 86 (2016) 434–442.
- [17] M.C. Darnell, J.Y. Sun, M. Mehta, C. Johnson, P.R. Arany, Z. Suo, D.J. Mooney, Performance and biocompatibility of extremely tough alginate/polyacrylamide hydrogels, Biomaterials 34 (2013) 8042–8048.
- [18] D. Gupta, D. Singh, N.C. Kothiyal, A.K. Saini, V.P. Singh, D. Pathania, Synthesis of chitosan-g-poly(acrylamide)/ZnS nanocomposite for controlled drug delivery and antimicrobial activity, Int. J. Biol. Macromol. 74 (2015) 547–557.
- [19] S. Saber-Samandari, S. Saber-Samandari, F. Ghonjizade-Samani, J. Aghazadeh, A. Sadeghi, Bioactivity evaluation of novel nanocomposite scaffolds for bone tissue engineering: the impact of hydroxyapatite, Ceram. Int. 42 (2016) 11055–11062.
- 20] S.C. Chao, M.J. Wang, N.S. Pai, S.K. Yen, Preparation and characterization of gelatinhydroxyapatite composite microspheres for hard tissue repair, Mater. Sci. Eng. C 57 (2015) 113–122.
- [21] S. Saber-Samandari, N. Nezafati, S. Saber-Samandari, The effective role of hydroxyapatite-based composites in anticancer drug-delivery systems, Crit. Rev. Ther. Drug 33 (2016) 41–75.
- [22] L. Morejón, J.A. Delgado, N. Davidenko, E. Mendizábal, E.H. Barbosa, C.F. Jasso, Kinetic effect of hydroxyapatite types on the polymerization of acrylic bone cements, Int. J. Polym. Mater. 52 (2003) 637–654.
- [23] J. Zhang, C. Wang, J. Wang, Y. Qu, G. Liu, In vivo drug release and antibacterial properties of vancomycin loaded hydroxyapatite/chitosan composite, Drug Deliv. 19 (2012) 264–269.
- [24] H. Liu, L.S. Taylor, K.J. Edgar, The role of polymers in oral bioavailability enhancement; a review, Polymer 77 (2015) 399–415.
- [25] A. Bohr, M. Yang, S. Baldursdóttir, J. Kristensen, M. Dyas, E. Stride, M. Edirisinghe, Particle formation and characteristics of celecoxib-loaded poly(lactic-co-glycolic acid) microparticles prepared in different solvents using electrospraying, Polymer 53 (2012) 3220–3229.
- [26] C.V. Rao, B.S. Reddy, NSAIDs and chemoprevention, Curr. Cancer Targets 4 (2004) 29–42.
- [27] S. Grosch, T.J. Maier, S. Schiffmann, G. Geisslinger, Cyclooxygenase-2 (COX-2)-independent anticarcinogenic effects of selective COX-2 inhibitors, J. Natl. Cancer Inst. 98 (2006) 736–747.
- [28] P. Pyrko, N. Soriano, A. Kardosh, Y.T. Liu, J. Uddin, N.A. Petasis, F.M. Hofman, C.S. Chen, T.C. Chen, A.H. Schonthal, Downregulation of survivin expression and concomitant induction of apoptosis by celecoxib and its non-cyclooxygenase-2-inhibitory analog, dimethyl-celecoxib (DMC), in tumor cells in vitro and in vivo, Mol. Cancer 5 (2006) 19.
- [29] J. Lin, P.W. Hsiao, T.H. Chiu, J.I. Chao, Combination of cyclooxygenase-2 inhibitors and oxaliplatin increases the growth inhibition and death in human colon cancer cells, Biochem. Pharmacol. 70 (2005) 658–667.
- [30] P.H. Hsiao, C.C. Chang, H.F. Liu, C.M. Tsai, T.H. Chiu, J.I. Chao, Activation of p38 mitogen-activated protein kinase by celecoxib oppositely regulates survivin and gamma-H2AX in human colorectal cancer cells, Toxicol. Appl. Pharmacol. 222 (2007) 97–104.
- [31] S. Saber-Samandari, S. Saber-Samandari, M. Gazi, F.C. Cebeci, E. Talasaz, Synthesis, characterization and application of cellulose based nano-biocomposite hydrogels, J. Macromol. Sci., Pure Appl. Chem. 50 (2013) 1133–1141.
- [32] R. Zhang, P.X. Ma, Poly(a-hydroxyl acids)/hydroxyapatite porous composites for bone-tissue engineering. I. Preparation and morphology, J. Biomed. Mater. Res. 44 (1999) 446–455.
- [33] D. Ashcroff, S. Chapman, W. Clark, S. Millson, Upper gastroduodenal ulceration in arthritis patients treated with celecoxib, Ann. Pharmacother. 35 (2001) 829–834.
- [34] A. Chime Salome, C. Onunkwo Godswill, I. Onyishi Ikechukwu, Kinetics and mechanisms of drug release from swellable and non swellable matrices: a review, Res. J. Pharm., Biol. Chem. Sci. 4 (2013) 97–103.
- [35] S. Saber-Samandari, M. Gazi, O. Yilmaz, Synthesis and characterization of chitosangraft-poly(n-allyl maleamic acid) hydrogel membrane, Water Air Soil Pollut. 224 (2013) 1624.
- [36] M. Ray, K. Pal, A. Anis, A.K. Banthia, Development and characterization of chitosan based polymeric hydrogel membranes, Des. Monomers Polym. 13 (2010) 193–206.
- [37] T.F. Jiao, J.Z. Zhou, J.X. Zhou, L.H. Gao, Y.Y. Xing, X.H. Li, Synthesis and characterization of chitosan-based schiff base compounds with aromatic substituent groups, Iran. Polym. J. 20 (2011) 123–136.
- [38] A. Zanotto, M.L. Saladino, D.C. Martino, E. Caponetti, Influence of temperature on calcium hydroxyapatite nanopowders, Adv. Nanopart. 1 (2012) 21–28.
- [39] S. Saber-Samandari, H.O. Gulcan, S. Saber-Samandari, M. Gazi, Efficient removal of anionic and cationic dyes from an aqueous solution using pullulan-graftpolyacrylamide porous hydrogel, Water Air Soil Pollut. 225 (2014) 2177.
- [40] S. Lee, M. Porter, S. Wasko, G. Lau, P.Y. Chen, E.E. Novitskaya, A.P. Tomsia, A. Almutairi, M.A. Meyers, J. McKittrick, Potential bone replacement materials prepared by two methods, Mater. Res. Soc. Symp. Proc. 1418 (2012) 177–188.
- [41] K. Rezwan, Q.Z. Chen, J.J. Blaker, A.R. Boccaccini, Biodegradable and bioactive porous polymer/inorganic composite scaffolds for bone tissue engineering, Biomaterials 27 (2006) 3413–3431.
- [42] S. Saber-Samandari, C.C. Berndt, K.A. Gross, Selection of the implant and coating materials for optimized performance by means of nanoindentation, Acta Biomater. 7 (2011) 874–881.

- [43] T. Boudou, O. Jacques, P. Catherine, T. Philippe, An extended relationship for the characterization of Young's modulus and Poisson's ratio of tunable polyacrylamide gels, Biorheology 43 (2006) 721–728.
- [44] S. Jana, S.J. Florczyk, M. Leung, M. Zhang, High-strength pristine porous chitosan scaffolds for tissue engineering, J. Mater. Chem. 22 (2012) 6291–6299.
- [45] V. Karageorgiou, D. Kaplan, Porosity of 3D biomaterial scaffolds and osteogenesis, Biomaterials 26 (2005) 5474–5491.
- [46] C.E. Mancini, C.C. Berndt, L. Sun, A. Kucuk, Porosity determinations in thermally sprayed hydroxyapatite coatings, J. Mater. Sci. 36 (2001) 3891–3896.
- [47] A. Zare-Harofteh, S. Saber-Samandari, S. Saber-Samandari, The effective role of akermanite on the apatite-forming ability of gelatin scaffold as a bone graft substitute, Ceram. Int. 42 (2016) 17781–17791.
- [48] C.T. Laurencin, L.S. Nair, Nanotechnology and Regenerative Engineering: The Scaffold, CRC Press, USA, 2014.
- [49] C. Changotade, G.R. Bostan, A. Consalus, F. Poirier, J. Peltzer, J.J. Lataillade, D. Lutomski, G. Rohman, Preliminary in vitro assessment of stem cell compatibility with cross-linked poly(ε-caprolactone urethane) scaffolds designed through high internal phase emulsions, Stem Cells Int. 2015 (2015) 283796.
- [50] M. Rani, A. Agarwal, Y.S. Negi, Review: chitosan based hydrogel polymeric beads- as a drug delivery system, Bioresources 5 (2010) 2765–2807.
- [51] V. Asadian-Ardakani, S. Saber-Samandari, S. Saber-Samandari, The effect of hydroxy-apatite in biopolymer-based scaffolds on release of naproxen sodium, J. Biomed. Mater. Res. B Appl. Biomater. (2016). http://dx.doi.org/10.1002/jbm.a.35838 (in press).

استفاده از تجهیزات مورد تایید شبکه آزمایشگاهی فناوری نانو در مقاله ISI

با توجه به آئین نامه حمایت از مقاله ISI، حمایت تشویقی مقالاتی که در آنالیز دادهها، تعیین مشخصات و تولید مواد از تجهیزات دستگاهی ساخت داخل استفاده کرده باشند، افزایش می یابد.

لازم است تجهیزات مورد استفاده جزء فهرست مورد تایید شبکه آزمایشگاهی فناوری نانو باشند، همچنین مشخصات دستگاه و نام شرکت سازنده نیز باید در متن مقاله، ذکر شده باشد.

مشخص کردن بخشی که در مقاله به دستگاه اشاره شده است.				
Biocompatible nanocomposite scaffolds based on copolymer-grafted chitosan for bone tissue engineering with drug delivery capability	عنوان مقاله			
Freeze Dryer, FD-10, Pishtaz Engineering Co., Iran	نام دستگاه			
722	شماره صفحه			
2	ستون			
4	پاراگراف			
2	سطر			

• مبلغ حمایت تشویقی در صورت استفاده از نام دستگاه و نام ایران در متن مقاله ۲۰ درصد و در صورت استفاده فقط از نام دستگاه در متن مقاله ۱۰ درصد افزایش می یابد.